Reviews of Electromagnetics, Vol. IV, 2025
EuCAP 2025 Special Issue
DOI: 10.53792/RoE/2025/25015

Reviews of Electromagnetics
EuCAP 2025 Special Issue

Profile-Reduced S/X-Band Shared-Aperture Antenna Array with Frequency-Selective Surfaces

Mohamed Räsänen[1], Juha Ala-Laurinaho[1], Andrea Di Giovanni[2], José Manuel Fernández Gonzalez[3], Alfonso Tomás Muriel-Barrado[4], Ville Viikari[1]

Abstract
Shared-aperture antennas (SAAs) are becoming more popular due to their desirable traits such as miniaturization and multi-band operation. However, achieving adequate SAA performance often requires a high total antenna profile or costly manufacturing. In this work, we review the state-of-the-art SAAs and present the design concept and simulation results of a novel dual-circularly polarized SAA for satellite communications. The S-band element is realized with a band-to-band isolating dipole, and the steerable X-band array utilizes slot antennas as radiating elements. An artificial magnetic conductor (AMC) reflector is employed to manage reflection phases, enabling a reduced total antenna profile of $0.083\,\lambda$ at the lowest operation frequency, and co-planar placement of the S-band and X-band elements. This architecture utilizes a single, cost-effective two-layer PCB shared by both the low-band and high-band radiating elements, reducing manufacturing costs and time. The SAA simulations indicate a –10-dB total active reflection coefficient bandwidths of 20.7% for the S-band and 13.7% for the X-band array broadside beam. The axial ratio (AR) is less than 1 dB for the broadside beam across the target band for both the S-band and X-band, and the AR remains below 3 dB for the X-band array when steering $\pm 40^\circ$ in the principal and diagonal planes.

Key terms
Artificial magnetic conductor, beamforming, frequency-selective surface, low profile, phased array, shared-aperture antenna

[1] *Aalto University, Department of Electronics and Nanoengineering, Espoo, Finland, mohamed.rasanen@aalto.fi*
[2] *SENER Aerospacial, Tres Cantos, Spain, andrea.digiovanni@aeroespacial.sener*
[3] *Universidad Politécnica de Madrid, E.T.S.I. Telecomunicación, Madrid, Spain, josemanuel.fernandez.gonzalez@upm.es*
[4] *Group of Radio-Frequency, Circuits, Antennas, and Systems (RFCAS), Department of Electronic and Communication Technologies, Universidad Autónoma de Madrid, 28049 Madrid, Spain, alfonsot.muriel@uam.es*
***Corresponding author**: mohamed.rasanen@aalto.fi

Received: 23/05/2025, Accepted: 01/09/2025, Published: 28/11/2025

1. Introduction

The requirements for cost, size reduction, and performance in modern wireless systems continue to escalate rapidly. For this reason, shared-aperture antennas (SAAs) have gained prominence in applications such as defense [1], space [2], communications [3], and radar [4]. SAAs integrate two or more elements for different frequency bands within a single radiating aperture, enabling miniaturization and potential cost savings. However, the design of SAAs is inherently more complex than single-band arrays due to space constraints, which pose challenges in achieving adequate band-to-band and intra-band isolation, bandwidth, and radiation performance. This work begins with a brief overview of state-of-the-art SAAs, describing various SAA concepts and discussing their tradeoffs. These designs typically employ traditional antenna elements such as dipoles, microstrip patch antennas (MPAs), dielectric resonator antennas (DRAs), and traveling-wave (TW) antennas.

Building on this review, we introduce a novel SAA design based on [5] that leverages frequency-selective surfaces (FSSs) and filtering techniques to address limitations of existing approaches. The proposed SAA features a filtering dipole antenna for the low-band (LB), operating at S-band (2.2–2.29 GHz), and a 4×4 rectangular slot antenna array for the high-band

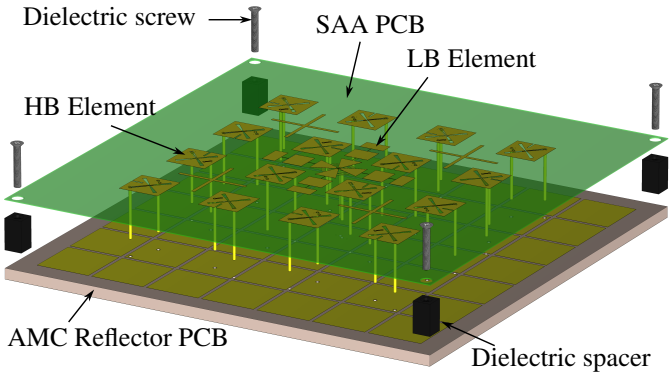

Figure 1: Illustration of the SAA concept of this work. The SAA is backed by an AMC reflector.

(HB), operating at X-band (8–8.4 GHz). These elements are co-located on a cost-effective two-layer PCB (RO4350B, $\varepsilon_r = 3.66$, $\tan\delta = 0.0037$), positioned above an artificial magnetic conductor (AMC) reflector (Alumina 96%, $\varepsilon_r = 9.4$, $\tan\delta = 10^{-4}$), as illustrated in Fig 1. The AMC reflector works as an FSS that provides the desired reflection phases for the radiating elements. The proposed design introduces several novel advancements:

1. **First co-planar integration of LB dipole and HB slots above an AMC:** For the first time, LB dipole and HB slot antennas (or any reflector-based elements) are co-located on the same plane above an AMC reflector, eliminating the need for complex interleaved and stacked designs that increase manufacturing time, complexity, and costs.
2. **First SAA with wide axial ratio (AR) bandwidth and beamwidth:** The design achieves excellent AR performance, maintaining a wide AR bandwidth and beamwidth for both S-band and X-band.
3. **First dipole-based SAA with ultra-low total profile:** The proposed SAA achieves a total profile of $0.083\,\lambda_L$, where λ_L is the lowest operating frequency. A first for dipole-containing SAAs, enabled by the altered reflection phase provided by the AMC.

To enhance band-to-band isolation in this compact co-planar arrangement, a dual-ring FSS element surrounds the dipole feeds, acting as a band-stop filter (BSF) for the X-band and a matching structure for the S-band. Additionally, the band-to-band isolation is enhanced by slotting the dipole arms to function as a low-pass stepped-impedance filter (SILPF) for the X-band. These filtering structures improve band-to-band isolation by more than 16 dB while maintaining all antenna elements on a low-cost two-layer PCB. The simulation results of the proposed design are compared with state-of-the-art SAAs, demonstrating its competitive performance while maintaining low complexity. The paper concludes with a discussion of the design's implications and future prospects for the proposed SAA development.

2. State of The Art

The art of antenna design is deeply influenced by the specific application requirements, as they dictate the performance, structure, complexity, and cost of the antenna. Certain applications necessitate broad bandwidth, while others require high isolation within a narrower frequency range. Some designs prioritize high directivity, whereas others demand an omnidirectional radiation pattern. This section serves as an overview for the state-of-the-art SAAs, where the performance and structural tradeoffs between the SAA topologies are investigated and compared. To align with the theme of this work, the review of state-of-the-art designs is organized from highest-profile to lowest-profile configurations.

2.1. Traveling-Wave SAAs

TW-antennas are well known for their unmatched wide-band characteristics, this feature is naturally retained in their SAA formation. For example, an SAA designed with horns [6], or Vivaldi elements [7] exhibit this trait. The horn SAA achieves bandwidths more than 16/28.5% for the LB and HB, whereas the SAA realized with Vivaldi elements reach 80.7/46.2% bandwidths. The Vivaldi SAA concept is illustrated in Fig. 2.

However, the cost of the wide bandwidth is a rather bulky, high-profile structure, which can be more than a wavelength at the LB frequency. Such designs can also be subject to moderately high manufacturing costs due to complex processes such as machining or metal 3D printing. Furthermore, TW-SAAs typically exhibit significant mutual coupling between elements due to the proximity of large LB and HB radiating apertures. This typically results in a band-to-band isolation of about 15 dB for state-of-the-art horn and Vivaldi-based SAAs [6, 7]. Moreover, particularly very wide-band horn and Vivaldi SAA designs often exhibit single-linear (SLIN) polarization. This stems from the large element size, which complicates the integration of the orthogonally polarized element within a constrained space. This limits their suitability for applications that require dual-linear (DLIN), single-circular (SC), or dual-circular (DC) polarizations.

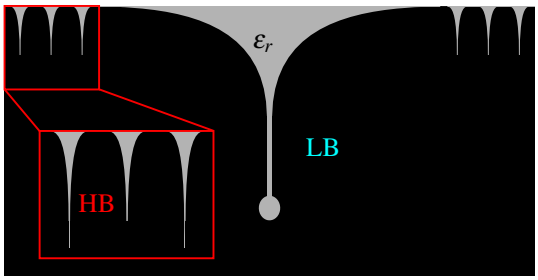

Figure 2: Example TW-SAA concept with Vivaldi elements, which is similar to the design in [7]. The grey color indicates the dielectric, and the black color denotes copper.

2.2. Dipole SAAs

Traditional dipoles are valued for their simplicity, predictable radiation patterns, efficiency, easy implementation of DLIN and DC polarizations, and ease of construction. Although not inherently wide-band, modern SAA designs achieve bandwidths greater than 15% for LB elements and more than 10% for HB elements through various feeding and matching techniques [3,8,9]. While dipoles are often fabricated on cost-effective two-layer PCBs, their total manufacturing cost for SAA implementations

can be high due to the need for interleaved LB and HB dipoles at different heights as shown in Fig. 3, requiring a complex assembly process.

This interleaved placement is required because traditional reflectors maintain a constant 180° reflection phase at the reflector surface across frequencies, unlike AMC reflectors, which can enable co-planar designs as will be discussed in Section 3.1. Consequently, the total profile height, dictated by the LB element, is typically $\sim 0.25\,\lambda_L$. Due to the high separation distance of LB and HB dipoles, dipole-based SAAs can achieve competitive isolation. For instance, in [8], a tri-band dipole SAA achieves a worst-case band-to-band isolation of about 25 dB through spatial separation of elements and filtering techniques.

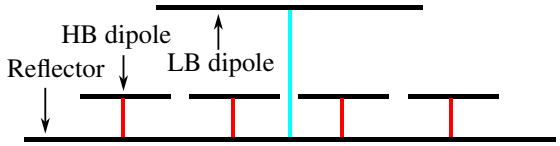

Figure 3: Example SAA concept with dipole elements as in [9]. In this example, each dipole is printed on individual PCBs.

2.3. Dielectric Resonator SAAs

DRAs are known for their compact size and wide bandwidth, which can be controlled by the dielectric permittivity, geometry of the DRA, and the feeding mechanism. Hence, DRAs can be considered as strong candidates for space-constrained antenna designs such as SAAs [10, 11]. DRAs can be desirably co-located on the same plane, as they typically do not require a dedicated reflector as shown in Fig. 4. Contrary to the TW-SAAs, achieving DLIN or DC polarization is also conveniently possible with DRAs, as the orthogonal polarizations can share the same DRA element while maintaining a compact form-factor.

Although the complexity of DR SAAs varies by design, a key common factor is the reliance on the dielectric properties of the resonator material to excite specific resonant modes. This often requires precise material selection and, in some cases, integration of external vertical feeding structures. In addition, they often need a PCB as a platform and for excitation, which can include several metal layers, thereby increasing total manufacturing costs and assembly complexity.

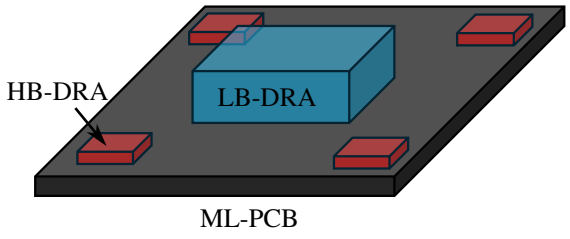

Figure 4: Example SAA concept with DRA elements. The ML-PCB includes the feeding structure for the DRA elements.

2.4. FSS-Based and Hybrid SAAs

Recently, new type of dipole-based SAAs, depicted in Fig. 5, that utilize FSSs have emerged in the literature [12–15]. In [12], an FSS was used to lower the profile of the DLIN polarized dipole SAA, where the total profile of the structure is about $0.14\,\lambda_L$, VSWR = 2. Furthermore, the worst-case band-to-band isolation reported is better than 20 dB. Although the profile was reduced while the performance of the SAA was maintained, the complexity is higher than SAAs utilizing only traditional reflectors due to the additional FSS layer between the LB and HB elements.

The FSS concept has also been used together with DRA elements for a steerable DLIN polarized tri-band SAA [16], where the achieved fractional bandwidths were 15/5.7/3.6%, while having a total profile of $0.14\,\lambda_L$ for the lowest operating frequency. The LB element utilizes the FSS for LB radiation, while the DRAs radiate in mid-band (MB) and HB. However, the manufacturing complexity is very high. The design includes multi-layer PCBs for feeding, baluns for the LB radiator, and 3D-printed DRAs with external feeding structures.

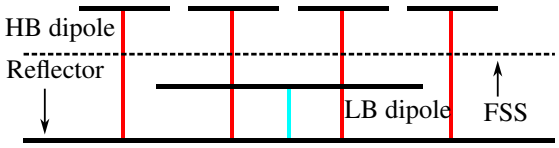

Figure 5: Example SAA concept from [12] with dipole elements and a decoupling FSS.

2.5. Multilayer PCB SAAs

Multilayer PCB antennas are known for their versatile design possibilities while maintaining compact form factor and achieving DLIN or circular polarization. MPAs in particular are one of the staple elementary building blocks in antenna array design, and the LB and HB elements can be co-located on the same PCB with relative ease as depicted in Fig. 6. Even though MPAs are generally known for their simplicity, achieving dual or circular polarization while maintaining sufficient isolation in their SAA form can require several PCB layers [2, 4, 17–19]. This increases the PCB manufacturing costs significantly [20]. However, the prototype assembly costs are typically lower compared to the other types of SAAs, if the PCB only requires the attachment of connectors. Typically, multilayer PCB SAAs exhibit a narrow bandwidth for the LB. For the cited works in this section, the profile is less than $0.1\,\lambda_L$, while the bandwidth in the LB is less than 10%.

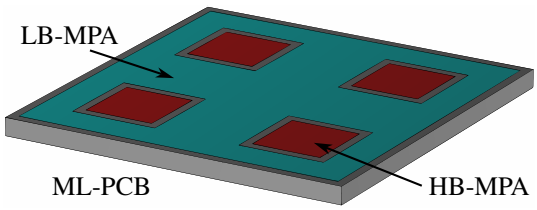

Figure 6: Example SAA concept with patch antennas. The HB patches (red) are embedded within the LB patch (blue).

2.6. Comparison of the State of The Art

The typical performance metrics and total profile heights of the discussed state-of-the-art SAAs are summarized in Table 1.

Dipole-based SAAs provide a balanced trade-off between profile and performance, while TW-SAAs offer the widest bandwidth but have the highest profile and typically support only SLIN polarization with the lowest band-to-band isolation. ML-PCB SAAs achieve the lowest profile, highest isolation through various integrated filtering structures, and simplest assembly, but are constrained by the narrowest bandwidth and potentially higher PCB manufacturing costs. DRA-based SAAs enable compact designs through dielectric-driven resonance, though they can require precise material selection and exhibit at least moderate assembly complexity and isolation metrics. Emerging dipole and hybrid SAAs with FSSs offer a reduced profile compared to traditional dipole SAAs, albeit with significantly increased design and manufacturing complexity.

Table 1: Typical achievable traits of modern SAA designs.

Technology	Profile (λ_L)	BW	Isolation	Complex.
TW	≈ 1	Widest	Lowest	Low
Dipole	≈ 0.25	Wide	High	High
Hybrid + FSS	≈ 0.14	Wide	High	Highest
DRA	≈ 0.14	Wide	Moderate	Moderate
ML-PCB	< 0.1	Narrow	Highest	Lowest

3. Proposed Design Concept

The proposed design belongs to the hybrid + FSS category, but reduces the total profile to $< 0.1\,\lambda_L$ and the complexity to low. As shown in Fig. 1, the proposed SAA concept integrates a 4×4 HB array comprised of dual-polarized slot antennas with the central dual-polarized LB dipole. The dipole and slot elements are placed on top of an AMC reflector to enable the coplanar placement of the LB and HB elements with reduced total antenna profile. The choice of HB slot antenna and LB dipole antenna is based on the diverse near-field distributions of the two elements. The HB element behaves as a magnetic dipole, whereas the LB element operates as an electric dipole. Compared to an all-dipole array, this can inherently yield better band-to-band isolation, despite the LB and HB elements being in very close proximity.

In this design, DC polarization is achieved by feeding the orthogonal ports individually. Hence, a 20-dB isolation between the orthogonal feed ports is considered sufficient to achieve an adequate AR below 3 dB for each element. To maintain AR performance during beamforming across a wide band, the HB elements are sequentially rotated to reduce cross-polarization, and cross-shaped decoupling structures are introduced between them. The cross-shaped decoupling structures slightly enhance the intra-band isolation at HB to further reduce AR.

Together with the element pattern, the steering performance of any array can be characterized through the well-known array factor

$$AF = \sum_{n=1}^{N} a_n e^{jk(x_n \sin\theta\cos\phi + y_n \sin\theta\sin\phi + z_n\cos\theta)}, \qquad (1)$$

where N denotes the number of elements, a_n is the excitation coefficient of element n, k is the wavenumber, and (x_n, y_n, z_n) denote the coordinates of element n.

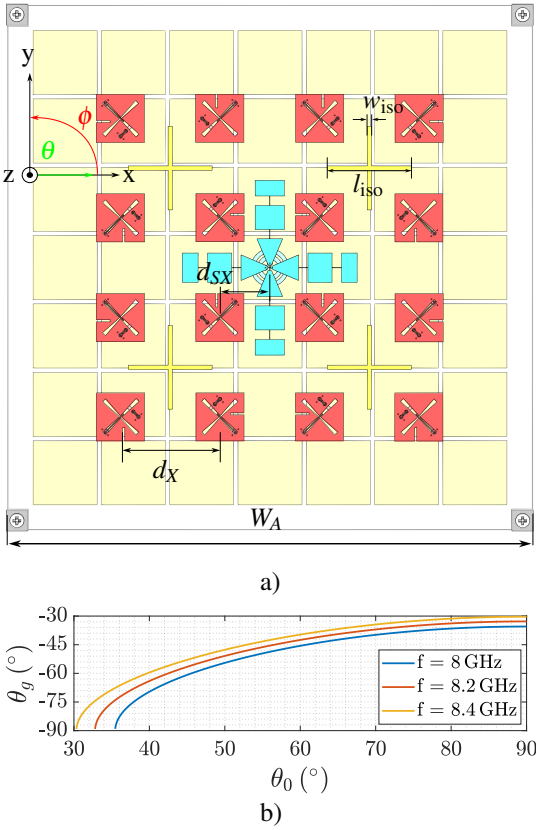

Figure 7: a) S/X-band SAA dimensions with one S-band element and 16 X-band elements, where $W_A = 125.9$ mm, $d_X = 23.9$ mm and $d_{SX} = 11.95$ mm. The intra-band isolation structure has values $w_{iso} = 1$ mm, and $l_{iso} = 20$ mm. b) Appearance angle of grating lobe maxima as a function of steering angle in principal steering planes for the target X-band frequencies.

The inter-element distance d_x of the HB elements is $0.67\,\lambda_H$, exceeding the typical grating-lobe (GL) free limit for scanning arrays. However, this limit is for an all-angle scanning array. The benefit of increasing the inter-element distance is increased array directivity. Additionally, it is also common for element-to-element isolation to improve. Hence, it can be beneficial to tailor the inter-element distance for the case-specific steering range, side lobe level (SLL) or grating lobe level (GLL), and achievable element pattern. The appearance angle of the GL maxima as a function of steering direction can be obtained by

$$\theta_g = \sin^{-1}\left(\sin\theta_0 + \frac{m\lambda}{d_e}\right), \qquad (2)$$

where $m = -1$ for the first GL. The SAA array arrangement and GL appearance angles as a function of main beam direction for the target frequency band is depicted in Fig. 7.

3.1. AMC Reflector

AMCs, a subset of FSSs, can be used to reduce antenna profiles by altering the reflection phase for single-element designs [21, 22] and SAAs [15, 23, 24]. However, prior work has not demonstrated major reductions in complexity and total antenna profiles for the SAAs with FSSs due to the interleaved

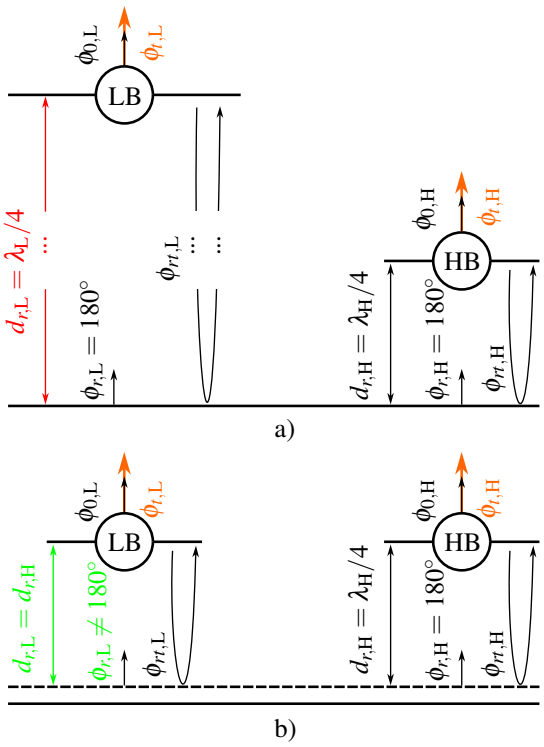

Figure 8: Conceptual SAA element arrangement for constructive interference, with a) traditional metal reflector, and b) proposed AMC reflector.

and stacked design approach. The reported total profiles of SAAs still remain well above $0.1\,\lambda_L$.

In this design, the AMC is implemented as a periodic surface realized with another two-layer PCB, which is engineered to alter the reflection phase of the incident waves such that constructive superposition is achieved towards the intended radiation direction for both the LB and HB elements. This superposition is desirable for matching the radiating elements and to obtain constructive superposition of fields towards the desired radiation direction. The operational principles of the SAA with both traditional perfect electric conductor (PEC) -like and AMC reflectors are depicted in Fig. 8. In this figure, ϕ_0 represents the initial phase of the transmitted wave,

$$\phi_{rt} = 2\,d_r(2\pi/\lambda) \tag{3}$$

denotes the phase shift accumulated by the wave during its round-trip from the radiating element to the reflector and back, ϕ_r is the phase introduced by the reflector upon reflection, and

$$\phi_t = \phi_0 + \phi_{rt} + \phi_r \tag{4}$$

is the total phase of the wave at the element plane, combining the initial and reflected phase contributions. For constructive interference between the initial and reflected waves in the desired frequency bands, the wrapped total phase must satisfy the condition $(\phi_0 - 90^\circ) \leq \phi_t \leq (\phi_0 + 90^\circ)$. With a traditional PEC-like reflector, the reflection phase $\phi_r = 180^\circ$ remains theoretically

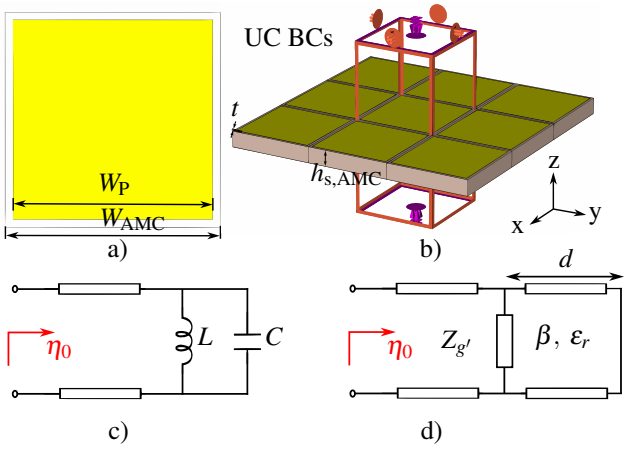

Figure 9: a) Planar AMC unit-cell (UC) geometry, b) the periodic boundary condition (BC) setup in CST MWS and the thickness dimensions of the AMC, c) equivalent circuit model of the AMC, where η_0 is the free-space impedance, and d) grid impedance transmission line model of the AMC according to [25].

constant across all frequencies upon reflection, this requires to adjust d_r for the band-respective elements separately. Hence, the AMC reflector is used to reduce the total antenna profile, manufacturing costs, and assembly complexity by co-locating the LB and HB antennas in the same plane. The AMC can be engineered to exhibit multi-band operation, and can theoretically be modeled as an equivalent circuit [26, 27], or as a grid impedance transmission line (TL) model [25]. While the circuit model is a simpler and faster approach, the grid impedance TL model also includes the harmonic effects. In this work, the AMC was designed for the LB with the circuit model approach, which was validated with unit cell simulations using CST MWS. The AMC geometry, simulation model, circuit model, and the grid impedance TL model are shown in Fig. 9.

The AMC achieves zero-phase reflection at the resonance frequency, which for a resonant LC circuit is determined as

$$f_r = \frac{1}{2\pi\sqrt{LC}}, \tag{5}$$

where the capacitance and inductance are determined by the geometry of the patch by

$$L = \mu_r\mu_0\,h_{s,AMC} \text{ and} \tag{6}$$

$$C = \frac{\varepsilon_r\varepsilon_0\,W_P}{\pi}\cosh^{-1}\left(\frac{W_{AMC}}{W_{AMC}-W_P}\right). \tag{7}$$

The reflection phase of the AMC for the LB from the circuit model can then be obtained with

$$\phi_r = \mathrm{Im}\left(\ln\left(\frac{Z_{AMC}-\eta_0}{Z_{AMC}+\eta_0}\right)\right), \tag{8}$$

where

$$Z_{AMC} = \left(X_L^{-1}X_C^{-1}\right)^{-1}. \tag{9}$$

As previously mentioned, the target is to obtain wrapped phase $(\phi_0 - 90^\circ) \leq \phi_t \leq (\phi_0 + 90^\circ)$ for both the LB and the HB to

Table 2: X-band antenna element dimensions

Parameter	d_c	d_{is}	d_v	L_f	l_{is}	l_{MS}	L_s	l_{TMS}	L_X	r_{AN}	r_{an}	r_c
Value (mm)	2.93	5	2	1.75	3.25	2	11.25	0.5	11.5	0.67	0.3	0.1
Parameter	W_C	W_f	W_{is}	W_{MS}	W_{s1}	W_{s2}	W_{s3}	r_f	r_v	s_{e1}	s_{e2}	W_{sf}
Value (mm)	0.2	0.15	0.5	0.75	0.3	0.45	1	0.3	0.15	0.123	0.25	0.5

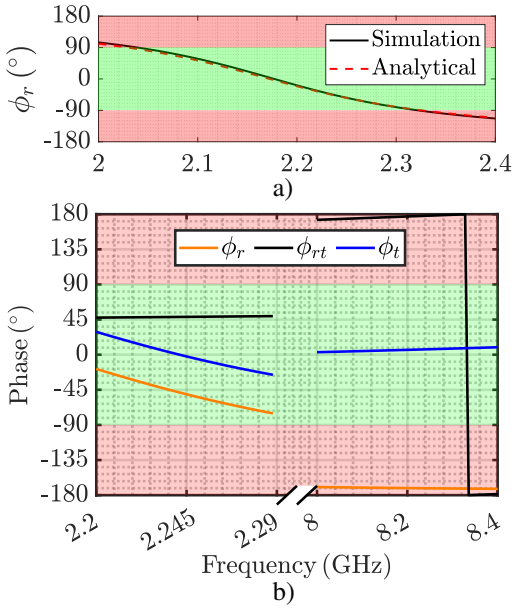

Figure 10: a) Simulated vs. analytical circuit model reflection phase of the AMC for the S-band, b) simulated ϕ_r, computed ϕ_{rt}, and computed ϕ_t of the AMC for $d_r = 9$ mm, $W_{AMC} = 16.4$ mm, $W_P = 15.4$ mm, $h_{s,AMC} = 3$ mm, and $t = 0.035$ mm.

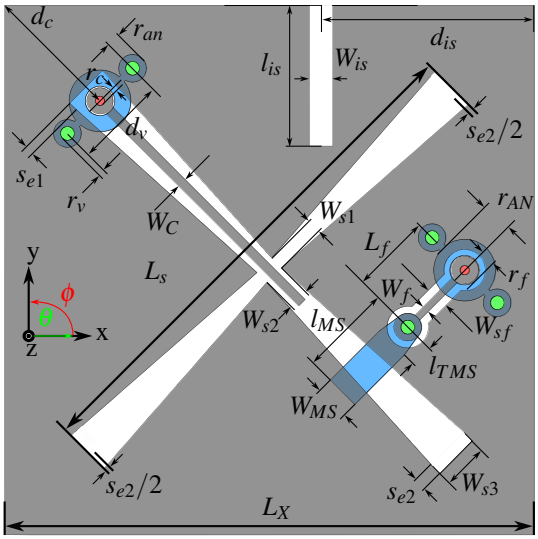

Figure 11: Final X-band element dimensions of the SAA. Grey color indicates the top copper layer and the blue color the bottom copper layer, respectively. Vias are indicated with green color, and the coaxial cable inner conductors with red color. The CPW excites the 45° polarization, and the MS the 135° polarization, respectively.

obtain constructive interference in the designated radiation direction of the SAA. In this AMC design, the reflection phase of the LB waves are engineered to achieve this feature, whereas the HB waves have a reflection phase of $\sim 180°$. Hence, the AMC effectively operates as a perfect magnetic conductor (PMC) for the LB and as a PEC-like reflector for the HB. This results in a trivial design process for the AMC, since one can focus the efforts on only altering the LB reflection phase.

The proposed arrangement enables the profile of the antenna height to be dictated by the HB frequency instead of the LB frequency. Therefore, the LB and HB elements are placed at a $\lambda/4$ distance at HB above the AMC reflector, which is ~ 9 mm at 8.2 GHz. Thus, the reflection phase for the LB was designed to be $\sim 50°$ to achieve wrapped $\phi_t \approx 0°$ at the center frequency of the LB. The simulation results of the FSS in conjunction with the computations indicate that the reflection phase is altered such that the desired constructive interference occurs for both LB and HB for $d_r = 9$ mm as shown in Fig. 10.

3.2. X-band Element

The HB element is a compact dual-polarized slot antenna, where the slots share the same junction to obtain near-mutual phase centers for the orthogonal polarizations. This is beneficial for achieving adequate AR performance in circular polarization applications, as co-located phase centers ensure a stable 90° phase difference across the beamwidth, minimizing angle-dependent phase errors.

However, achieving a dual-polarized slot antenna with a shared junction on the same PCB layer poses a challenge due to poor isolation between the orthogonal ports. Since the slots share the same junction, fields can easily couple between the two slots at the junction point. This problem was addressed in [28], where co-located microstrip (MS) and coplanar waveguide (CPW) feeds were used to excite the two orthogonal slots, achieving a measured isolation better than 30 dB with a bandwidth greater than 6%. The HB element in this work utilizes a similar concept for the X-band, albeit with additional modifications:

1. The bandwidth is improved to 15% by tapering the slots.
2. By adding an isolation slot, the simulated isolation is maintained at better than 27 dB even with the presence of a reflector.
3. The feeding structure is modified to allow for vertical coaxial cable feeding.

The proposed slot antenna used in the HB array is shown in Fig. 11, and its dimensional values are displayed in Table 2. Following the design modifications, the performance of the element is characterized through its S-parameters, radiation pattern, AR, and modal analysis. These metrics validate the antenna's

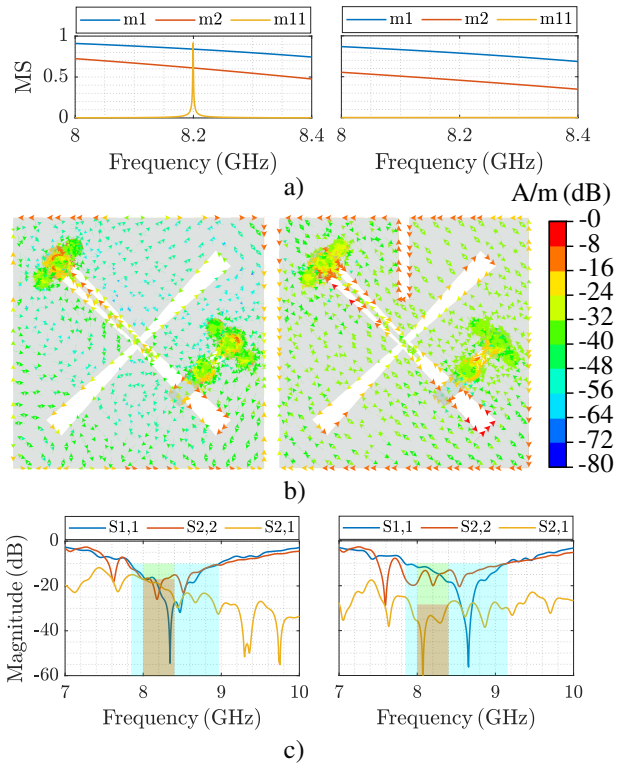

Figure 12: Comparisons for the slot antenna elements without the isolation slot (left), and with isolation slot (right) for a) modal significance, b) normalized surface current distribution of coupling mode 11, and c) S-parameters.

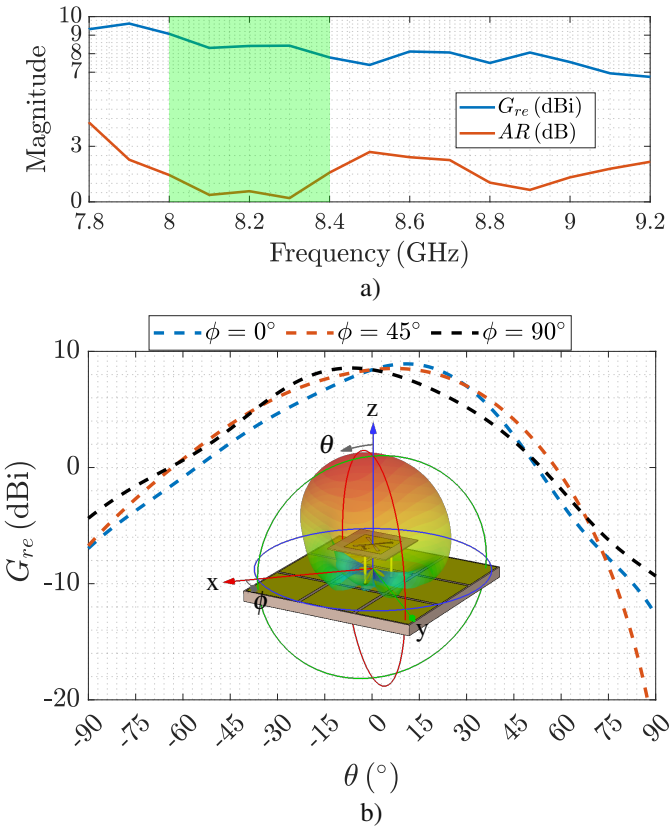

Figure 13: a) Broadside RHCP realized gain and AR of the HB element, and b) RHCP realized gain patterns of the HB element. The broadside AR is below 3 dB within 7.9–9.2 GHz.

suitability for circularly-polarized operation, particularly for applications requiring low AR.

The shared junction supports a common mode that facilitates cross-coupling, degrading isolation to below 20 dB without the isolation slot. The isolation slot disrupts this mode by altering the current distribution, effectively suppressing the unwanted resonance. Modal analysis in Fig. 12a reveals the absence of the undesired eigenmode in the modified structure, while Fig. 12b shows the mode's surface current distributions. Since the AMC operates as a PEC-like reflector for the HB element, a PEC reflector was used in the modal analysis. The antenna operates over a 15% bandwidth in the X-band as shown in Fig. 12c, where the reflection coefficients for both orthogonal ports are below −10 dB. The isolation between the orthogonal ports exceeds 27 dB even with the presence of the reflector, due to the isolation slot suppressing cross-coupling at the shared junction.

When fed with coefficients for circular polarization, a gain of approximately 9 dBi is obtained towards the broadside across the target band, while the AR is maintained well below 3 dB as shown in Fig. 13a. The stable and low AR performance is explained by the shared slot junction and high isolation of the HB element. Furthermore, the 3-dB beamwidth is almost 80° at the center frequency as shown in Fig. 13b, which partially determines the steering range of the X-band array.

3.3. S-band element

The LB printed dipole element is designed without a separate balun to minimize costs and manufacturing complexity. Although the diverse field distributions between the dipole and slot antennas yield moderate isolation, the very close proximity of the dipole and slot antennas results in relatively high coupling. Hence, two filtering mechanisms are introduced to the dipole to reduce band-to-band coupling:

1. The dipole arms are slotted so that they act as a SILPF for the HB.

2. A dual-ring FSS element is introduced around the dipole feed points, operating as a matching structure for the dipole and a BSF for the HB.

The SILPF and BSF filtering cut-off and resonance frequencies can initially be characterized with an equivalent circuit or TL model before full-wave simulations. The band-to-band isolation to a nearby HB element, and the surface current distributions of the traditional and proposed filtering dipole are presented in Figs. 14a and b. The surface current distribution shows the self-cancellation of the coupled HB currents on the LB filtering dipole in Fig. 14b, resulting in an improvement of more than 16 dB in band-to-band isolation as shown in Fig. 14c. Without the filtering structures, a higher-order mode is excited on the dipole arms, causing unwanted radiation and significantly

Table 3: Values of the S-band element dimensions.

Parameter	d_g	L_d	l_e	l_i	l_{ms1}	l_{ms2}	l_p	l_t	r_{AS}	r_{bs1}	r_{bs2}
Value	1.3	41.75	3.75	2.25	1	0.29	5.75	6.77	0.2	0.345	0.63
Parameter	r_c	r_{i1}	r_{i2}	r_{o1}	r_{o2}	r_{VS}	w_{t1}	w_{t2}	w_i	w_{MS}	W_p
Value	0.1	2	3.55	2.95	4.5	0.075	0.8	6.13	0.08	0.125	7

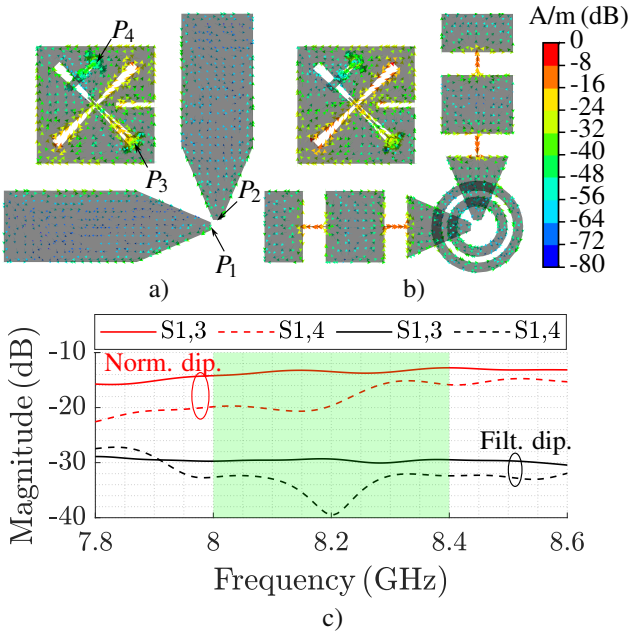

Figure 14: Normalized coupled surface current distributions from port 3 of the slot to the arms of the a) baseline dipole antenna, and b) proposed filtering dipole antenna at 8.2 GHz, c) coupling between the LB dipole and HB slot at X-band.

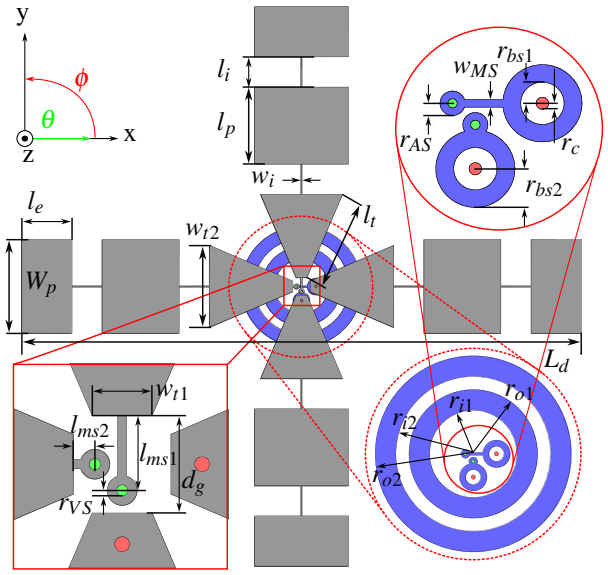

Figure 15: S-band element dimensions. Grey color indicates the top copper layer and the blue color the bottom copper layer, respectively. Vias are indicated with green color, and the coaxial cable inner conductors with red color.

higher band-to-band coupling. Together with the dipole dimensions, the dual-ring FSS element also aids in impedance matching by essentially adding inductance to the dipole's input impedance. The final design is shown in Fig. 15, and its respective dimensional values in Table 3.

3.4. SAA Performance

The excitation coefficients for circular polarization and beam steering were obtained with

$$a_p(\theta,\phi,\vec{u}_\alpha) = c\vec{E}_p^*(\theta,\phi)\cdot\vec{u}_\alpha^*, \tag{10}$$

where c is a scaling coefficient, E_p is the port-wise radiated electric field, and u_α is the polarization vector. The polarization vector is defined as

$$\vec{u}_\alpha = \frac{1}{\sqrt{2}}(\vec{u_\theta} \pm j\vec{u_\phi}), \tag{11}$$

which is used for generating excitation coefficients for circular polarization in MATLAB post-processing. The active reflection coefficient (ARC) for the S-band element with circular polarization coefficients was obtained with

$$\Gamma_{A,m} = \sum_{n=1}^{N} S_{mn}\frac{a_n}{a_m}, \tag{12}$$

where N is the number of ports, $a_{n/m}$ are the excitation coefficients for the ports n and m, and S_{mn} are the coupling coefficients. Ports 1 and 2 are the S-band ports (m), and ports 3–34 are the X-band ports. The total active reflection coefficient (TARC) is used to determine the impedance bandwidth, which is computed by

$$\Gamma_T = \sqrt{\frac{\sum_{n=1}^{N}|b_n|^2}{\sum_{n=1}^{N}|a_n|^2}}, \tag{13}$$

where b_n is the scattered signal. Due to the high isolation between the orthogonal ports indicated in Fig. 16a, the −10-dB Γ_T bandwidth is 20.7% ranging from 2.055–2.530 GHz for the S-band dipole as shown in Fig. 16b. The band-to-band coupling envelope $C_{S,X}$ shown in Fig. 16c was obtained from passive S-parameters, and describes the worst-case passive coupling between the S- and X-band elements. A very low coupling envelope was achieved for the target S-band, having a maximum value of −47.2 dB, and a maximum value of −28.4 dB for the target X-band. As shown in Fig. 17a, the S-band dipole achieves a maximum gain of 5.9 dBi toward the broadside while maintaining the AR below 1 dB across the target frequencies. The 3-dB AR beamwidths for the S-band center target frequency are more than 42° in the diagonal cut and more than 98° in the principal cuts, as shown in Fig. 17b. The 3-dB realized gain beamwidths are more than 75° for the principal cuts and 71° for the diagonal cut, as displayed in Fig. 17c.

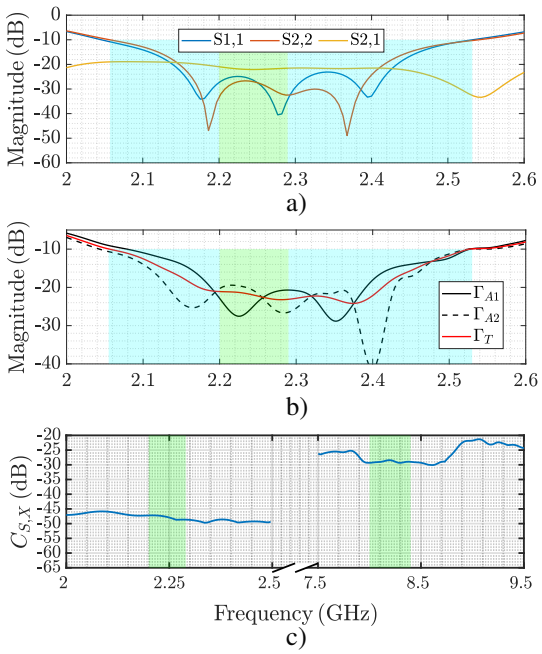

Figure 16: a) Passive S-parameters of the LB filtering dipole, b) ARCs and TARC of the LB dipole, when fed with LHCP excitations, c) passive coupling envelope between the S-band element ports and X-band array ports.

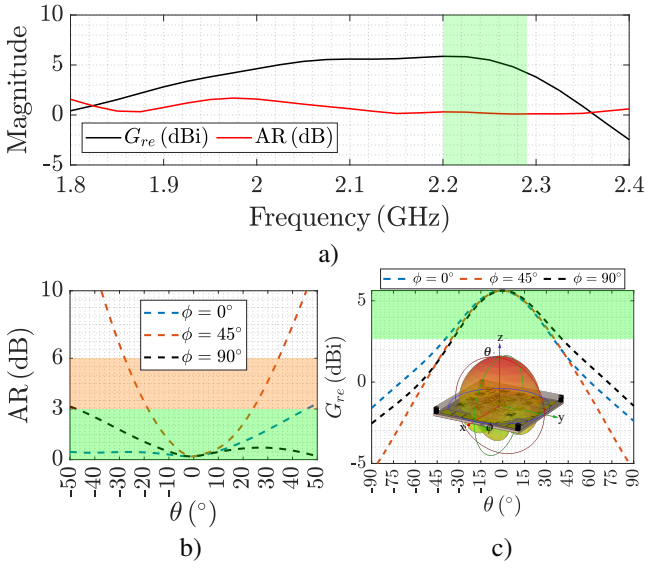

Figure 17: S-band element a) LHCP realized gain and AR across frequency, b) ARs at 2.245 GHz for the principal and diagonal cuts, and c) LHCP realized gains for the same cuts.

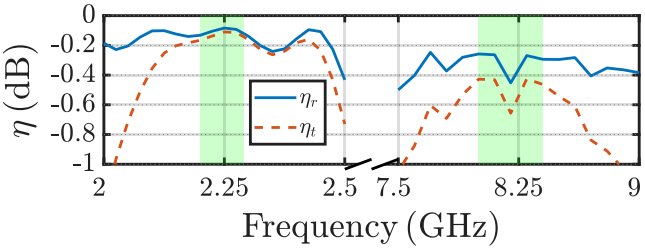

Figure 18: Broadside beam radiation (η_r) and total (η_t) efficiencies for the S-band element and X-band array.

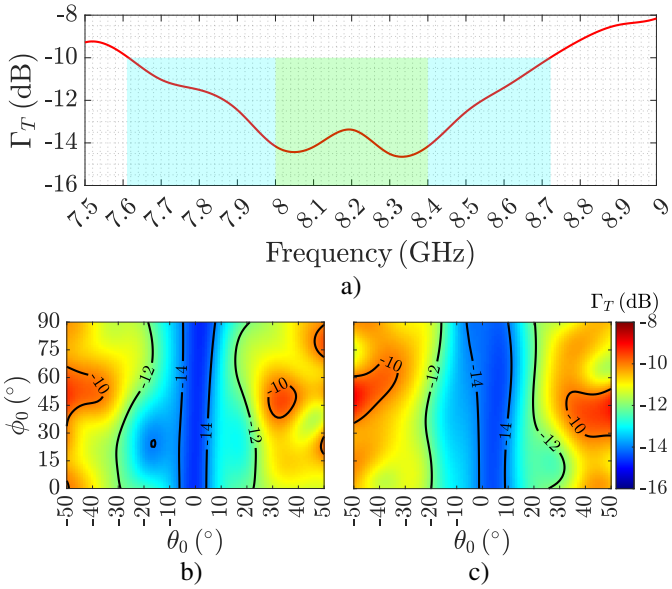

Figure 19: RHCP TARCs of the X-band array for a) broadside beam across frequency, and as a function of steering angle for b) 8 GHz, and c) 8.4 GHz.

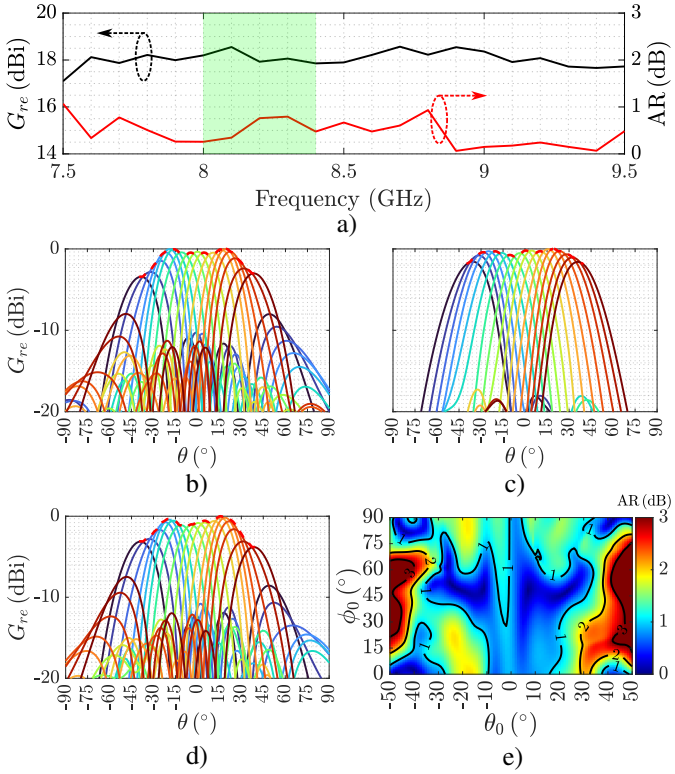

Figure 20: RHCP Realized gain of the X-band array for a) broadside beam across frequency, and when the beam is steered between $\theta_0 = -40°...40°$ at 8.2 GHz for the cuts b) $\phi = 0°$, c) $\phi = 45°$ d) $\phi = 90°$, and e) RHCP AR as a function of steering angle at 8.2 GHz.

The radiation and total efficiencies for the broadside beam are shown in Fig. 18, where the worst-case radiation efficiencies are −0.14 dB for the target S-band, and −0.45 dB for the target X-band. The respective values for the total efficiencies are −0.17 dB, and −0.66 dB. Although the simulated efficiency

Table 4: Performance comparison of relevant SAAs

Work	Tech.	Profile (λ_L)	N.o Bands	BW (%)	Isol. (dB)	Pol.	Gain (dBi)	Steerable?	Comp.
This[a]	**Hybrid**	**0.08**	**2**	**20.7/13.7**[b]	**47/28**	**DCP**	**5.9/18.6**[c]	**2D** ($\pm$**40**°)	**Low**
[6]	TW	>1	2	$>16/25$	15	SLIN	14.9/20.8[c]	No	Mod.
[7]	TW	>1.2	2	80.7/46.2	$>15/27$	SLIN	8.3/7	1D ($\pm$30°)	Low
[8]	Dipole	0.27	3	15.7/21.1/11.1	$>27/25/17$	DLIN	6.3/6.8/7.3	2D (N/A)	High
[9]	Dipole	<0.23	2	$>32.7/11.1$	N/A	DLIN	7.3/13	2D (N/A)	High
[10]	DRA	0.13	2	10.8/6.4	$>22/20$	SLIN	5.5/6.2	No	Mod.
[11][a]	DRA	0.20	2	51.4/24.3	N/A	SLIN	N/A	2D (N/A)	Mod.
[12]	Dipole+FSS	0.14	2	32.7/33.3	$>35/25$	DLIN	9.8/9.3	2D (N/A)	High
[14]	Dipole+FSS	0.14	2	$>32.7/14.1$	N/A	DLIN	9/8.4	2D (N/A)	High
[15]	Dipole+FSS	0.15	2	37.6/70.8	34/30	DLIN	9.2/8.4	2D (N/A)	High
[16]	DRA+FSS	0.14	3	15/5.7/3.6	N/A	DLIN	$>6/6/7.9$	1D ($\pm$55°)	High
[17]	ML-PCB	0.04	2	7.4/12.1	$>45/40$	SLIN	6.9/14.6[a,c]	1D ($\pm$30°)	Low

Only **total** antenna profiles are presented except for [8], including reflector and PCB thicknesses when applicable.
Tech. is technology, Isol. is band-to-band isolation, and Comp. is assembly complexity.
[a] Denotes simulated values
[b] Values obtained from -10 dB TARC bandwidth.
[c] Denotes array gain.

values are very competitive, longer coaxial cables employed during the prototyping phase are expected to introduce a marginal reduction in efficiency due to increased resistive losses and potential impedance mismatches. The X-band array TARC for the broadside beam is better than -10 dB across the 13.4% bandwidth, as shown in Fig. 19a, and the TARC is better than -9.1 dB when scanning the circularly polarized beam within $\phi_0 = -90°...90°$, $\theta_0 = -40°...40°$ as shown in Figs. 19b and c. The simulated maximum broadside RHCP realized gain of the HB array is 18.6 dBi within the target band, as shown in Fig. 20a, and the scan loss is about 3 dB when steering the beam in the principal and diagonal planes as indicated in Figs. 20b–d. The axial ratio is maintained below 1 dB for the broadside beam across the target frequencies and below 3 dB when steering the beam in the principal and diagonal planes as indicated in Fig. 20e.

4. Performance Comparison

Table 4 presents a comparative analysis of the proposed SAA design with state-of-the-art counterparts in the literature. Multilayer PCB-based SAAs achieve total profiles below 0.1 λ_L, but their LB bandwidth typically falls below 10%. Dipole-based SAAs exhibit profiles nearly three times larger than the proposed design with greater manufacturing complexity, whereas TW-SAAs have profiles larger by more than an order of magnitude while only exhibiting SLIN polarization. The proposed design not only rivals the band-to-band isolation of most state-of-the-art designs in the HB, but also outperforms all of them in the LB. While most state-of-the-art designs support beam steering, it was not demonstrated for many of them. It can be observed that the proposed SAA design exhibits competitive simulated performance in terms of profile, bandwidth, isolation, beam steering range, and gain, while maintaining low assembly complexity.

5. Conclusion

This work addressed critical trade-offs in SAA technologies, including profile height, bandwidth, isolation, and fabrication complexity. Existing TW, DRA, and dipole-based SAAs often achieve wide bandwidths at the cost of elevated profiles or complex structures, while FSS-integrated designs reduce form factor but compromise manufacturing cost and simplicity. ML-PCB SAAs offer high isolation and low profiles but require costly manufacturing and exhibit narrow bandwidths.

To overcome these challenges, a dual-band, polarization-reconfigurable S/X-band SAA was introduced, integrating a novel planar filtering dipole and a slot antenna array over an AMC reflector. The low-complexity AMC reflector adjusts the reflection phase for the LB radiator, enabling a total profile of 0.083 λ_L dictated by the HB frequency. The design achieves simulated -10-dB TARC bandwidths of 20.7% for the LB and 13.7% for the HB. Radiation metrics demonstrate robust circular polarization, with ARs below 1 dB in broadside directions for both bands, a 3-dB AR beamwidth of more than 98° for the LB dipole's principal cuts, and a 3-dB AR scan range of $\pm$40° for the X-band array. Circularly polarized maximum realized gains reach 5.9 dBi for the LB element and 18.6 dBi for the HB array. Despite the close proximity of co-located LB and HB elements on the same plane, band-to-band isolation exceeds 47 dB in the LB and 28 dB in the HB, enabled by embedded BSF and SILPF structures in the LB dipole.

The presented results were achieved without multilayer PCBs or complex assemblies, ensuring manufacturability, cost efficiency, and scalability. This approach provides a compelling solution for compact, dual-band antenna systems in spaceborne and terrestrial applications, such as SATCOM terminals and next-generation wireless infrastructure. Future work will explore tri-band extensions, prototype fabrication, and experimental validation under realistic conditions.

6. Acknowledgments

This work was supported by HPY Research Foundation, Business Finland through RF Sampo (3071/31/2021) and RF ECO3 (5665/31/2024) projects, ESA through NGAAGS project (4000138412/22/NL/AS), and the Spanish Government, Ministerio de Ciencia, Innovación y Universidades, under the project New Array Antenna Technologies and Digital Processing for the FUTURE Integrated Terrestrial and Space-based Millimeter Wave Radio Systems - UPM-InTerSpaCE (PID2020- 112545RB-C51) funded by MICIU/ AEI /10.13039/501100011033. The authors would like to thank Dr. Carolina Tienda Herrero from ESA for discussions on the ground station antenna requirements. Research infrastructure provided by Aalto Electronics-ICT was utilized for this work.

References

[1] T. A. Axness, R. V. Coffman, B. A. Kopp, and K. W. O'Haver, "Shared aperture technology development," *Johns Hopkins APL Technical Digest*, vol. 17, no. 3, pp. 285–294, 1996, [Online]. Available: https://secwww.jhuapl.edu/techdigest/content/techdigest/pdf/V17-N03/17-03-Axness.pdf [Accessed: Oct. 17, 2024].

[2] D. E. Serup, R. J. Williams, S. Zhang, and G. F. Pedersen, "Dual S- and X-band shared aperture antenna for nanosatellite applications," in *2021 15th Eur. Conf. Antennas Propag (EuCAP)*, Dusseldorf, Germany, 2021, pp. 1–5.

[3] S. He, X. R. Q. Wang, and X. Li, "A dual-polarization common-aperture antenna array for 2G/3G/4G/5G base stations," in *2021 13th Int. Symp. Antennas Propag. EM Theory (ISAPE)*, Zhuhai, China, 2021, pp. 1–3.

[4] P. Su, R. Shen, and D. Sun, "Design of an S/X dual-band shared aperture antenna array," in *2021 CIE Int. Conf. Radar (Radar)*, Haikou, Hainan, China, 2021, pp. 2728–2731.

[5] M. Räsänen, J. Ala-Laurinaho, A. Di Giovanni, J. M. Fernandez Gonzalez, A. T. Muriel-Barrado, and V. Viikari, "Profile-reduced S/X-band shared-aperture antenna array with frequency-selective surfaces," in *2025 19th Eur. Conf. Antennas Propag (EuCAP)*, March 2025, pp. 1–5.

[6] J. Yang, Z. Cao, H. Meng, Q. Li, and Y. Li, "A mutually enhanced Ka/W dual-band shared-aperture horn antenna," *IEEE Trans. Antennas Propag.*, vol. 72, no. 2, pp. 1234–1240, 2024.

[7] J. Ren, M. Zuo, B. Zhang, X. Du, Z. Chen, Y. Liu, and Y. Z. Yin, "Large frequency ratio vivaldi antenna system with low-frequency gain enhancement utilizing dual-function taper slot," *IEEE Trans. Antennas Propag.*, vol. 70, no. 6, pp. 4854–4859, 2022.

[8] W. Niu, B. Sun, and X. Huang, "A filtering and electromagnetic-transparent antenna for triple-band aperture-shared base station antenna array," *IEEE Antennas Wireless Propag. Lett.*, vol. 23, no. 1, pp. 244–248, 2024.

[9] W. Niu, B. Sun, G. Zhou, and Z. Lan, "Dual-band aperture shared antenna array with decreased radiation pattern distortion," *IEEE Trans. Antennas Propag.*, vol. 70, no. 7, pp. 6048–6053, 2022.

[10] X.-Y. Cheng, C. Ding, and R. W. Ziolkowski, "Dual-band shared-aperture dielectric resonator antenna (DRA) with suppressed cross-band interactions," *IEEE Trans. Antennas Propag.*, vol. 72, no. 7, pp. 5694–5704, July 2024.

[11] L. Yi, M. Li, M.-C. Tang, D. Sun, Q. Huang, and G. Ma, "Composite Ku/Ka wide-band dielectric resonator antenna elements with shared aperture," in *2024 IEEE 12th Asia-Pac. Conf. Antennas Propag. (APCAP)*, Sep. 2024, pp. 1–2.

[12] Y. Zhu, Y. Chen, and S. Yang, "Decoupling and low-profile design of dual-band dual-polarized base station antennas using frequency-selective surface," *IEEE Trans. Antennas Propag.*, vol. 67, no. 8, pp. 5272–5281, Aug 2019.

[13] L. Feng, H. Li, C. Wu, J. Yang, J. Qiu, A. Sihvola, and J. Qi, "Radiative deep-subwavelength frequency-selective surface-based cross-band decoupling method for base station antenna," *IEEE Trans. Antennas Propag.*, vol. 73, no. 2, pp. 771–781, Feb 2025.

[14] H. Li, J. Xu, Y. Nan, Q. Chen, and C. Zhou, "Low-profile dual-band shared-aperture base station antennas based on FSS radiators," *IEEE Antennas Wireless Propag. Lett.*, vol. 23, no. 6, pp. 1894–1898, June 2024.

[15] P. Du, Y. Cao, W. Che, and Q. Xue, "Low-profile dual-band dual-polarized aperture-shared antenna array using bifunctional metasurface," *IEEE Trans. Antennas Propag.*, pp. 1–1, 2025.

[16] Y. Sun, J. Zhang, P. Mei, S. Luo, W. Fu, and S. Zhang, "Tri-band dual-polarized shared-aperture antenna arrays with wide-angle scanning and low profile for 5G base stations," *IEEE Trans. Antennas Propag.*, vol. 72, no. 3, pp. 2455–2467, March 2024.

[17] X.-H. Ding, W.-W. Yang, H. Tang, L. Guo, and J.-X. Chen, "A dual-band shared-aperture antenna for microwave and millimeter-wave applications in 5G wireless communication," *IEEE Trans. Antennas Propag.*, vol. 70, no. 12, pp. 12 299–12 304, 2022.

[18] B. Kim and W. Hong, "A completely overlapped Ku- and Ka-band dual-polarized phased array for simultaneous terrestrial and satellite communications," in *2024 18th Eur. Conf. Antennas Propag (EuCAP)*, March 2024, pp. 1–5.

[19] D. Pozar and S. Targonski, "A shared-aperture dual-band dual-polarized microstrip array," *IEEE Trans. Antennas Propag.*, vol. 49, no. 2, pp. 150–157, Feb 2001.

[20] A. Vardya, "Factors affecting the cost of PCB fabrication," [Online]. Available: https://www.circuitnet.com/news/uploads/4/Factors_Affecting_the_Cost_of_PCB_Fabrication.pdf. [Accessed: Oct. 17, 2024].

[21] A. P. Feresidis, G. Goussetis, S. Wang, and J. C. Vardaxoglou, "Artificial magnetic conductor surfaces and their application to low-profile high-gain planar antennas," *IEEE*

Trans. Antennas Propag., vol. 53, no. 1, pp. 209–215, 2005.

[22] Y. Wang, J. Huang, Q. Yu, C. Zhou, W. Zhang, Y. Li, and H. Wong, "A low-profile multiband shared-aperture antenna using multiplexed metasurface," *IEEE Antennas Wireless Propag. Lett.*, vol. 24, no. 2, pp. 349–353, 2025.

[23] A. Volkov, V. Kakshin, I. Ryzhov, K. Kozlov, A. Kurochkin, and A. Grinev, "A low-profile dual-band shared-aperture antenna based on artificial magnetic conductor with transparent elements," *Microw. Opt. Technol. Lett.*, vol. 62, 06 2020.

[24] Y. Li and Q. Chu, "Artificial magnetic conductor-backed dual-band shared-aperture antenna array for base station applications," *Int. J. RF Microw. Comput.-Aided Eng.*, vol. 32, 06 2022.

[25] O. Luukkonen, C. Simovski, G. Granet, G. Goussetis, D. Lioubtchenko, A. V. Räisänen, and S. A. Tretyakov, "Simple and accurate analytical model of planar grids and high-impedance surfaces comprising metal strips or patches," *IEEE Trans. Antennas Propag.*, vol. 56, no. 6, pp. 1624–1632, June 2008.

[26] J. H. Yoon, E. Y. Kim, Y. Lim, and Y. J. Yoon, "Equivalent circuit model and reflection phase control methods for dual-band AMC," in *Proceedings of the 5th Eur. Conf. Antennas Propag (EuCAP)*, April 2011, pp. 1222–1226.

[27] A. Fattouche, L. Mouffok, S. Hebib, and A. Mansoul, "A triple band artificial magnetic conductor: Design & analytical model," *Prog. Electromagn. Res. Lett.*, vol. 104, pp. 161–168, 01 2022.

[28] X. Qin and Y. Li, "Compact dual-polarized cross-slot antenna with colocated feeding," *IEEE Trans. Antennas Propag.*, vol. 67, no. 11, pp. 7139–7143, 2019.